Research Letter **DOI:** 10.15541/jim20250064

Achieving High Power Density in Paper-based Piezoelectric Nanogenerators through Dual-phase BCZT Doping Strategy

WANG Siting[1], SUN Zixiong[1], LIU Xinying[1], HAN Peiqiao[1], WANG Xiuli[2], ZHANG Sufeng[3]

(1. School of Electronic Information and Artificial Intelligence, Shaanxi University of Science and Technology, Xi'an 710021, China; 2. Engineering Research Center of Eco-friendly Polymeric Materials, Ministry of Education, (Sichuan University), Chengdu 610065, China; 3. College of Bioresources Chemical & Materials Engineering, Shaanxi University of Science and Technology, Xi'an 710021, China)

Abstract: Development of high performance, flexible piezoelectric nanogenerators (PENGs) is critical for advancing self-powered sensing and microelectronic applications. In this study, a hydrogen-bond substitute strategy was employed to fabricate a multi-layer PENG based on a cellulose/polyvinylidene fluoride (PVDF) blend film matrix, incorporating multi-phase BCZT ($0.1BaZr_{0.2}Ti_{0.8}O_3$-$0.9Ba_{0.7}Ca_{0.3}TiO_3$) ceramic fillers. Structural characterization *via* SEM and TEM revealed that an intricate hydrogen-bond network facilitated the uniform dispersion of ceramic fillers within the composite film's sub-layers. In order to study the effect of filler distribution on piezoelectric performance, the single- and double-layer composite films with varying BCZT configurations were produced and evaluated. The results demonstrated that double-layer PENGs exhibit significantly enhanced electrical output compared to their single-layer counterparts, with the D-L_3H_7 configuration achieving an open circuit voltage (V_{OC}) of 23.13 V and a short circuit current (I_{SC}) of 8.32 μA. This enhancement is attributed to increased inter-layer interfaces, which effectively suppressed charge injection and migration, leading to improved charge density. Additionally, the presence of sharp tipped hexagonal tetragonal phase nanoparticles induced an electric field enhancement effect, further optimizing performance.

Key words: piezoelectric nanogenerator; cellulose; BCZT; hydrogen bond engineering strategy

Micro-nano electronic devices, such as wireless sensor nodes, wearable electronics, and implantable medical devices, have become more common because of the rapid advancement of science and technology[1-5]. These devices are often required to function autonomously in complex, dynamic environments, relying heavily on power sources. Traditional battery-powered devices, however, face significant limitations, such as finite battery life, the need for frequent replacements, and the large size and weight of batteries, which impede miniaturization and portability[6-10]. In response to these challenges, PENGs have emerged as a promising solution. PENGs convert ambient mechanical energy, such as human motion and vibrations, which allows for self-powered operation, reducing dependence on traditional batteries and lowering maintenance costs. The widespread application of PENGs is crucial for advancing the development of micro-nanoelectronic devices, particularly in the Internet of Things era, facilitating the development of intelligent and sustainable technologies[11-12].

PENGs combining polymers and ceramics offer superior performance compared to all-organic devices, due to the synergistic effects of both materials[13]. For example, Huang *et al*.[14] created a single-layer nanocomposite membrane by incorporating multi-walled carbon nanotubes (CNTs) into PVDF and polyacrylonitrile (PAN), which enhances piezoelectric and triboelectric effects. Rana *et al*.[15] created porous PVDF films using zinc oxide (ZnO) nanoparticles, resulting in an increase of 11% in output current and an increase of 8% in output voltage compared to pure PVDF-based PENGs. Despite these advancements, the reliance on organic materials in

Received date: 2025-02-18; **Revised date:** 2025-04-28; **Published online:** 2025-06-05
Foundation item: National Natural Science Foundation of China (52472132); Opening Project of Engineering Research Center of Eco-friendly Polymeric Materials, Ministry of Education (EFP-KF2403); Innovation Service Capability Support Plan of Xianyang (Science and Technology Innovation Talents)
Biography: WANG Siting (1999–), female, Master candidate. E-mail: wst11902023@163.com
王斯婷(1999–), 女, 硕士研究生. E-mail: wst11902023@163.com
Corresponding author: SUN Zixiong, associate professor. E-mail: sunzx@sust.edu.cn
孙梓雄, 副教授. E-mail: sunzx@sust.edu.cn

PENGs necessitates the use of organic solvents, contributing to environmental pollution[16-19]. Therefore, there is an increasing need for environmentally friendly materials. PENG applications benefit from the renewable characteristics, environmental friendliness, biocompatibility, low cost, mechanical strength, and inherent piezoelectricity of cellulose, a naturally polymeric material[20]. PVDF is flexible and can be formed into various shapes, adapting to numerous applications, including wearable and flexible electronic devices[21-25], due to its strong C–F bonds and piezoelectric β phase[26-27]. For example, Li *et al*.[28] enhanced the piezoelectric output of PVDF/cellulose acetate composites to 7.5 V and 2.1 μA, which was significantly higher than that of pure PVDF. Venkatesan *et al*.[29] used cellulose nanocrystals in PVDF blends to increase environmental friendliness and improved the piezoelectric output to 20.3 V and 1.2 μA. In these studies, single-layer composite films were prepared, limiting the structure design of the PENG and impeding the improvement of its output performance[30-31]. The authors' prior work constructed a PENG based on hydrogen bond engineering networks, and prepared a 0-3-0 composite film with better output than single-layer ones, but its output still lags due to a single filler. Thus, to further enhance the output performance, fillers with higher piezoelectric properties were added into the cellulose and PVDF mixed matrix.

In the realm of energy and materials science, the quest for highly efficient, cost effective, and high performance materials along with their preparation methods is of utmost importance. This study focuses on ceramic composite films made of BCZT ($0.1BaZr_{0.2}Ti_{0.8}O_3$-$0.9Ba_{0.7}Ca_{0.3}TiO_3$) ceramic composite films. A simple and low cost solid-state method was employed, where the sintering temperature was adjusted to fabricate cubic and tetragonal BCZT ceramics for realizing the co-doping of biphasic BCZT in composite films and exploring their properties. Additionally, the tape casting method was utilized to construct a bilayer composite film featuring a hydrogen-bond network structure. BCZT ceramics with different crystal phases were doped into distinct sub-layers to investigate the impact of different components within the same phase on the output performance. This approach breaks through traditional constraints, furnishing novel solutions for piezoelectric energy harvesting technology. As a result, the output performance of PENG devices is enhanced. It has great potential to play a crucial role in self-powered systems, wearable electronic devices, and other fields, leading to advancements in related technologies.

BCZT-based ceramics are frequently employed as fillers in polymer composites because of their outstanding dielectric properties and high composition tunability[32-36]. In this work, a simple and low-cost solid-phase method was introduced. By adjusting the sintering temperature, cubic and tetragonal BCZT ceramics were prepared as fillers, resulting in the co-doping of dual-phase BCZT ceramics in composite films. Then, using the tape casting method, a double-layer composite film with a hydrogen bond network structure was constructed. To examine the effect of different components in the same phase on output performance, BCZT ceramics with different crystal phases were divided into different sub-layers. The study found that the output power induced by electromechanical coupling of the PENG prepared based on dual-phase ceramic fillers and double-layer structure is significantly higher than that of the PENG prepared with single-phase BCZT ceramic fillers and single-layer structure composite films, achieving an improvement in output performance.

1 Experimental

The details of the experimental process of this work are provided in the supporting materials.

2 Results and discussion

2.1 Morphology and structure

In this study, CP-BCZT films with various structures were fabricated to have the same overall thickness, as presented in Fig. S1. Based on the contents of the tetragonal and cubic ceramic phases incorporated, they are labeled as follows: D-L, where the ceramic filler consists entirely of low-temperature-fired cubic-phase BCZT; D-H, with all high-temperature-fired tetragonal-phase BCZT as the filler; D-L_3H_7, indicating a 3 : 7 ratio of low-temperature-fired cubic-phase to high-temperature-fired tetragonal-phase BCZT (subsequent samples D-L_5H_5 and D-L_7H_3 follow the same naming convention). Meanwhile, Figs. S1(b1-b3) display double-layer films. These are named S-L_3H_7, denoting a 3 : 7 ratio of the low-temperature-fired cubic-phase to the high-temperature-fired tetragonal-phase BCZT, and this same 3 : 7 ratio applies to the thickness of each sub-layer relative to the total film thickness (subsequent samples S-L_5H_5 and S-L_7H_3 are named accordingly). The structures and performances of PENGs with different configurations are shown in Tables S1 and S2 of the supporting materials. The sharp diffraction peaks of BCZT crystals, synthesized by the solid-phase method[37], clearly indicate excellent crystallinity[38]. This is evidenced by a highly ordered atomic arrangement with strong periodicity and minimal

lattice defects. Fig. 1(a1) shows that BCZT prepared at high temperature is the tetragonal phase, while Fig. 1(a2) indicates that BCZT prepared at low temperature is cubic phase[39]. Eight peaks can be found in the diffraction patterns at $2\theta\approx22.1°$, 31.5°, 39.1°, 47.2°, 51.8°, 56.1°, 66.1°, and 74.7°, and they correspond to crystal planes of (100), (110), (111), (200), (210), (211), (220), and (310)[40]. In XRD patterns near 45° for tetragonal BCZT ($c\neq a$), (002) and (200) diffraction peaks split (citation), showing low symmetry. Cubic BCZT ($a=b=c$) has a single peak (200), with characteristic (111) and (220) peaks. These differences distinguish the two phases. Fig. 1(b) presents the Fourier transform infrared (FT-IR) spectrum of the thin film. Peaks at ~886 and 1404 cm^{-1} are characteristic of PVDF[41]. The peak at 3600 cm^{-1}, caused by hydroxyl stretching, is stronger in the double-layer film, indicating an interfacial hydrogen-bond network[42-44]. In BCZT, peaks at 497.23 and 1430 cm^{-1} are observed from Ti–O bending, which indicates good polarization[45]. Figs. 1(c1-c4) are the actual photos of S-L_3H_7, S-L_5H_5, D-L_3H_7, and D-L_5H_5, respectively. All films are transparent, indicating their significant potential for practical applications.

The morphological structure of the BCZT@cellulose/PVDF composite film was characterized using scanning electron microscope (SEM) and transmission electron microscope (TEM). The cross-sectional SEM image of the two-layer composite film D-L_3H_7, depicted in Fig. S2(a1), demonstrates high density resulting from the refined casting technique. Notably, there are no pores between adjacent sub-layers. There are discernible interfaces, presenting a unique double-layer structure. The energy-dispersive X-ray spectroscopy (EDS) maps corresponding to the red region in Fig. S2(a1) are presented in Figs. S2(a2-a6). Elements C, O, F, Ti, and Zr are uniformly distributed and denoted by different colors. The distribution pattern of elements C, O, and F, characteristic of PVDF, is slightly different from that of the ceramic filler. A more uniform and compact distribution can be observed in Figs. S2(a2-a4), which reveal the distribution of PVDF and cellulose around the ceramic particles. The TEM image in Fig. S2(b1) clearly presents ceramic particles (manifested as bright white spots). The spherical ones represent cubic-phase BCZT ceramic particles, while the hexagonal ones signify tetragonal-phase BCZT ceramic particles[46-47], indicating the successful integration of two distinct crystalline phases of BCZT into the composite film. The EDS spectra in Figs. S2(b2-b7) display elements C, O, F, Ba, Ti, and Ca. The cross-sectional EDS analysis reveals a homogeneous distribution of BCZT ceramic particles without significant agglomeration, consistent with the SEM results. Thus, the favorable dispersion of the ceramic filler within the cellulose and PVDF matrix is validated.

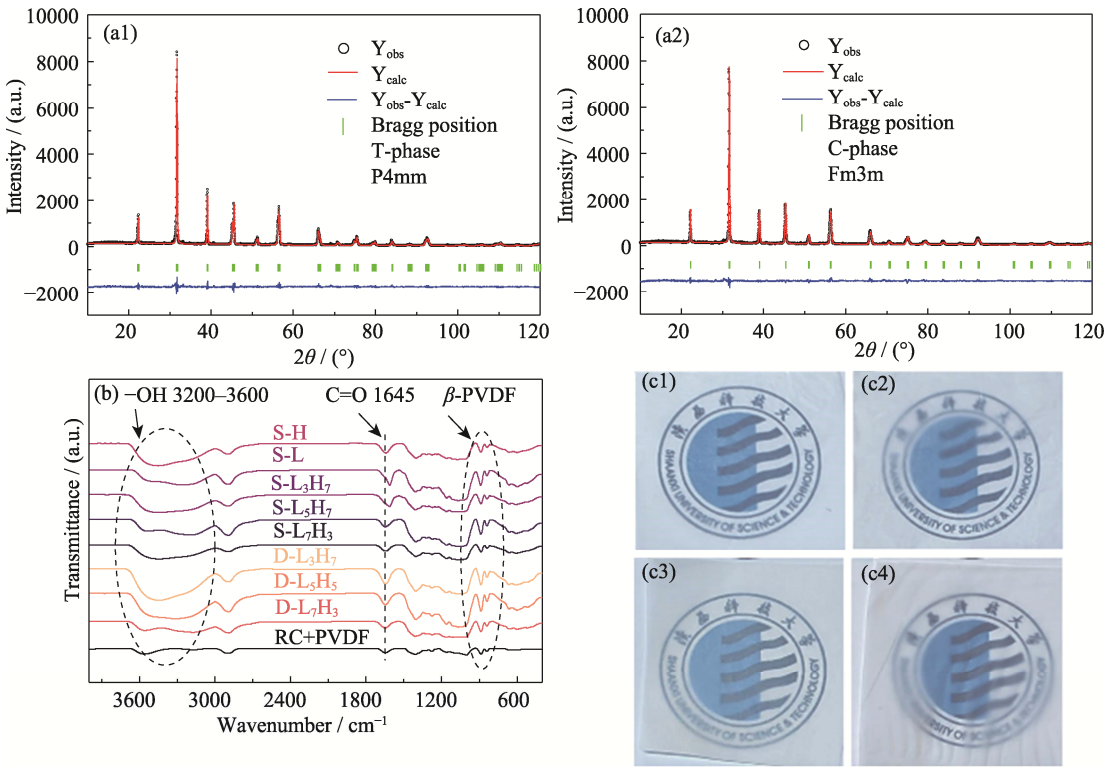

Fig. 1　XRD patterns and FT-IR spectra of the two-phase powders, as well as the physical pictures of the sample films
(a, b) XRD refined patterns of (a1) T-phase BCZT (tetragonal-phase) and (a2) C-phase (cubic-phase) BCZT; (b) FT-IR spectra of all films; (c1-c4) Real photos of (c1) S-L_3H_7, (c2) S-L_5H_5, (c3) D-L_3H_7, and (c4) D-L_5H_5

2.2 Electrical properties and characterization of composite films

In order to study the effects of BCZT ceramic particles with different crystal phases and composite film structures on the performance of PENG, the V_{OC} and I_{SC} of PENG were measured. Under a 20 N external force and 3 Hz frequency, the single-layer S-H composite film achieves the highest output. Figs. 2(a1, a2) show its 19 V V_{OC} and 4 μA I_{SC}. As the proportion of spherical cubic BCZT prepared at low temperature increases, the performance of PENG decreases[48]. In contrast, PENG's performance is significantly improved by hexagonal tetragonal BCZT prepared at high temperature[49]. Therefore, the shape of nanoparticles will affect the interface polarization and thus the performance of PENG. Under the same conditions, the performance of PENG prepared by double-layer film D-L_3H_7 is shown in Figs. 2(b1, b2), with a V_{OC} of 23.13 V and a I_{SC} of 8.32 μA. Similar to single-layer films, its performance decreases with the reduced tetragonal BCZT content. However, double-layer films are superior to single-layer ones. This is because the internal electric field is dominant in the double-layer film, and increasing the interface area will increase the charge density[50]. Secondly, separating the two-phase BCZT in different layers reduces the polarization cancellation effect inside the PENG[51]. With the increase of the content of high-performance tetragonal phase BCZT, this effect is further weakened, thereby enhancing the piezoelectric performance of the dual-layer nanogenerator.

Figs. S3(a1, a2) show the dielectric constant and dielectric loss of single-layer and double-layer films under different test conditions. Under the same test conditions, these parameters vary with the change of BCZT crystal phase ratio. This stems from BCZT's inherent properties, dipole polarization, and interfacial effects[52]. When the doped BCZT ceramics are prepared at high temperature, the dielectric constant of the single-layer structure film is 25.8 with a low loss of 0.13. In the double-layer structure film, the interlayer interface and hydrogen bond network increase the dielectric constant[53]. Specifically, at high frequencies (10^4), dielectric relaxation reduces the dielectric constant and raises loss; at low frequencies (10^{-4}), stability is maintained. So, the performance of PENG can be improved by adding BCZT ceramics with different phases to reduce dielectric loss and increase dielectric constant[54]. Figs. S3(b1, b2) display the dielectric temperature profiles of single- and double-layer films. As temperature increases, the dielectric constant decreases and the dielectric loss rises, possibly due to the redistribution of interfacial charge. Figs. S3(c1, c2) illustrate the electric hysteresis loops of single and double-layer composite films. Unlike typical rectangular electric hysteresis loops, these loops are elliptical. This results from reversible and irreversible polarization factors during external force induced polarization, leading to remnant polarization and energy loss[55].

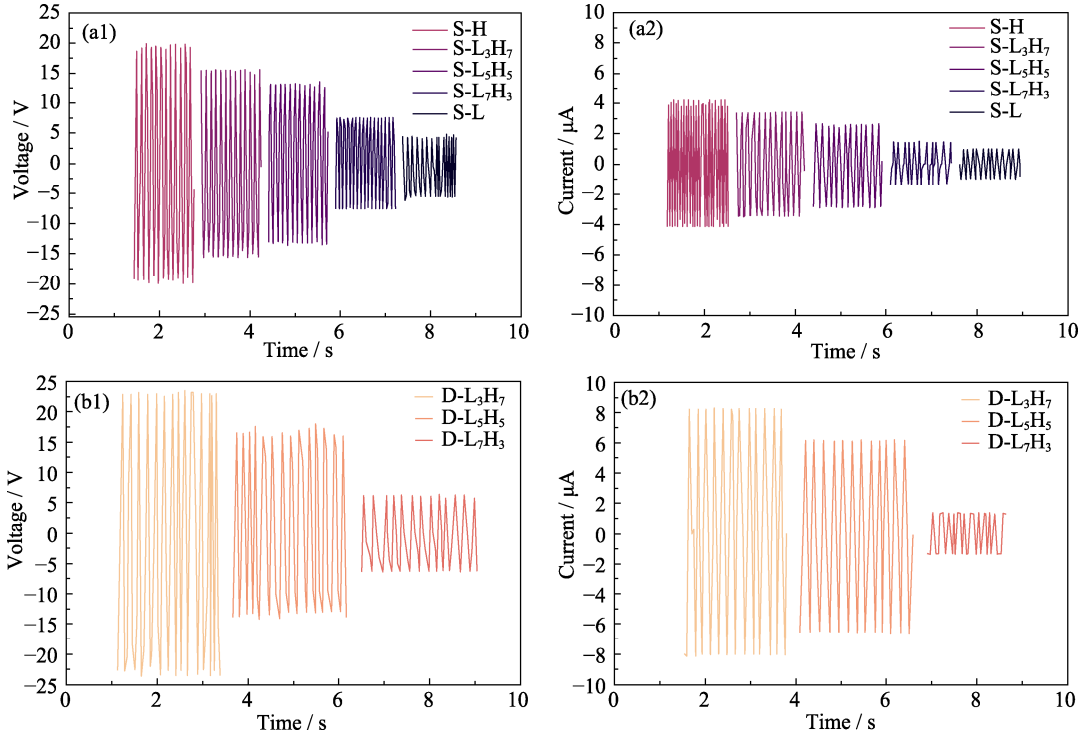

Fig. 2 Performance tests of PENGs with different configurations

(a1) V_{OC} and (a2) I_{SC} of PENGs fabricated based on different single-layer composite films at 20 N/3 Hz; (b1) V_{OC} and (b2) I_{SC} of PENGs fabricated based on different double-layer composite films at 20 N/3 Hz. Colorful figures are available on website

2.3 Mechanical properties and characterization of composite films

Fig. S4 shows the water contact angle and mechanical properties of composite films. Figs. S4(a1-a5) show water contact angle test results for single-layer films, while Figs. S4(b1-b3) show results for double-layer ones. All films have water contact angles >90°, indicating water repellency, which is beneficial for practical applications. Fig. S4(c) presents stress-strain curves[56]. Double-layer films have better mechanical properties. "Zig-zag" crack path propagation, a common failure mode, is blocked by inter-layer interactions[57]. The Young's modulus shown in Fig. S4(d) was calculated from Fig. S4(c). The double-layer D-L_3H_7 has a tensile strength of 110 MPa and an elongation at break of 38%, showing that multi-layer structures can boost cellulose-based film mechanical properties.

2.4 Application and stability test

The D-L_3H_7 PENG is highly flexible and sensitive, rapidly responding to diverse deformations with minimal hysteresis. This characteristic provides significant potential for wearable applications to detect human motions that involve large strains and high bending angles. A 3.5 cm×3.5 cm×5 mm PENG device was attached to the index finger knuckle, wrist, and elbow. As depicted in Figs. 3(a1-a3), different output signals are generated at different bending angles. With increasing bending angles, the tensile stress on the device grows, resulting in noticeable signal differences in the range of 0°–30°, 0–60° and 0°–90°, and indicating its potential for human health monitoring. In addition, different exercise behaviors can also be predicted by the amplitude of the V_{OC}, as demonstrated in Fig. 3(a4). This reveals a strong correlation between the output of the D-L_3H_7 PENG and deformation. Consequently, it can function as a self-powered motion sensor, and independently detect human joint and body movements. Its ability to precisely distinguish motion ranges holds great promise for human healthcare and activity-tracking applications. The device's mechanical stability and reliability were confirmed through continuous impact tests. As shown in Fig. S5(a), after 400 s of mechanical tapping at 3 Hz, the output voltage of D-L_3H_7 PENG remains relatively stable, with a 1% fluctuation, as shown in Figs. S5(b, c). This indicates its suitability for harvesting energy from sporadic vibrations in daily life.

3 Conclusions

In this study, a hydrogen-bond replacement strategy was employed to fabricate a multi-layer PENG using a cellulose/PVDF blend film as the matrix and a

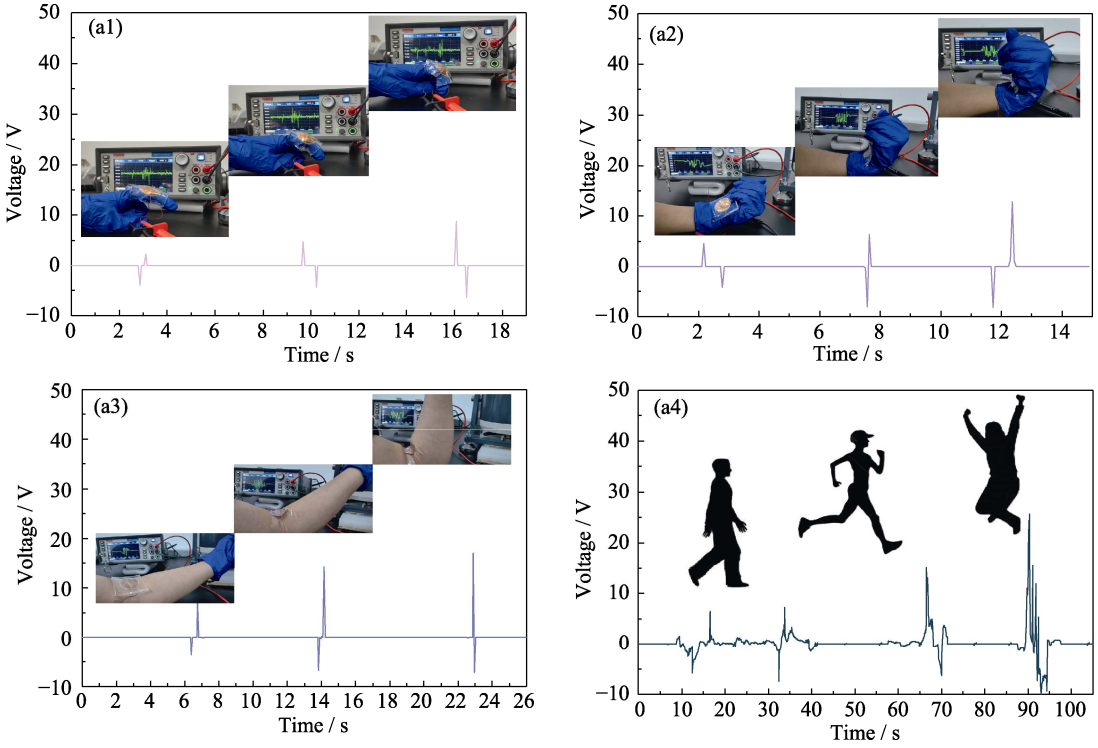

Fig. 3　Monitoring of various human motions in real-time

Output voltage as function of time for a typical D-L_3H_7 PENG at (a1) different finger joint bending (30°, 60°, and 90°) motions, (a2) different wrist joint bending (30°, 60°, and 90°) motions, (a3) different elbow joint bending (30°, 60°, and 90°) motions, and (a4) walk, run, and skip deformations

multi-phase BCZT ceramic powder as the filler. Structural analyses *via* SEM and TEM confirmed that a complex hydrogen-bond network facilitated the uniform dispersion of the ceramic fillers within the composite film's sub-layers. Single- and double-layer composite films with varying BCZT configurations were fabricated and evaluated to elucidate the influence of filler distribution on device performance. The results demonstrated that double-layer PENGs exhibited significantly enhanced electrical output compared to their single-layer counterparts. In particular, the D-L_3H_7 configuration achieved a maximum V_{OC} of 23.13 V and a I_{SC} of 8.32 μA. This enhancement is attributed to the increased inter-layer interfaces, which effectively suppressed charge injection and migration, leading to a higher charge density. Furthermore, the hexagonal tetragonal phase nanoparticles within the D-L_3H_7 structure likely contributed to an enhancement of the electric field, further optimizing performance. This study proposed flexible, cost-effective, and ergonomically designed PENGs that demonstrate significant potential for real-time human motion sensing and future applications in flexible microelectronics.

Supporting Materials

Supporting materials related to this article can be found at https://doi.org/10.15541/jim20250064.

References:

[1] HAN J, WANG M, ZHAO T, *et al*. Triboelectric nanogenerator based on graphene forest electrodes. *Journal of Inorganic Materials*, 2019, **34(8):** 839.

[2] ZHOU X, Li C, WU D, *et al*. Recent advances of cellular stimulation with triboelectric nanogenerators. *Exploration*, 2023, **3(4):** 20220090.

[3] ANNAMALAI P K, NANJUNDAN A K, DUBAL D P, *et al*. An overview of cellulose‐based nanogenerators. *Advanced Materials Technologies*, 2021, **6(3):** 2001164.

[4] ZHANG Y, GAO X, WU Y, *et al*. Self-powered technology based on nanogenerators for biomedical applications. *Exploration*, 2023, **1(1):** 90.

[5] GUO Y, CHEN Z, WANG H, *et al*. Progress of inorganic filler based composite films for triboelectric nanogenerators. *Journal of Inorganic Materials*, 2021, **36(9):** 919.

[6] WABG B, WEI X, ZHOU H, *et al*. Viscoelastic blood coagulation testing system enabled by a non-contact triboelectric angle sensor. *Exploration*, 2023, **4(1):** 20230073

[7] CHEN Y, GAO Z, ZHANG F, *et al*. Recent progress in self-powered multifunctional e-skin for advanced applications. *Exploration*, 2022, **2(1):** 20210112.

[8] RAM F, GUDADHE A, VIJAYAKANTH T, *et al*. Nanocellulose reinforced flexible composite nanogenerators with enhanced vibrational energy harvesting and sensing properties. *ACS Applied Polymer Materials*, 2020, **2(7):** 2550.

[9] WANG X, ZHU Y, PENG Z, *et al*. Phase structure and piezoelectric property of $(Ba_{0.85}Ca_{0.15})(Ti_{0.9}Zr_{0.1-x}Sn_x)O_3$ lead-free piezoceramics. *Journal of Inorganic Materials*, 2022, **37(5):** 513.

[10] NAN B, ZANG J, LU W L, *et al*. Recent progress on additive manufacturing of piezoelectric ceramics. *Journal of Inorganic Materials*, 2022, **37(6):** 585.

[11] VULLERS R J M, VAN SCHAIJK R, DOMS I, *et al*. Micropower energy harvesting. *Solid-State Electronics*, 2009, **53(7):** 684.

[12] MARZENCKI M, AMMAR Y, BASROUR S. Integrated power harvesting system including a MEMS generator and a power management circuit. *Sensors and Actuators A: Physical*, 2008, **145:** 363.

[13] YUAN X, GAO X, YANG J, *et al*. The large piezoelectricity and high power density of a 3D-printed multilayer copolymer in a rugby ball-structured mechanical energy harvester. *Energy & Environmental Science*, 2020, **13(1):** 152.

[14] HUANG A, ZHU Y, PENG S, *et al*. Improved energy harvesting ability of single-layer binary fiber nanocomposite membrane for multifunctional wearable hybrid piezoelectric and triboelectric nanogenerator and self-powered sensors. *ACS Nano*, 2023, **18(1):** 691.

[15] RANA M M, KHAN A A, HUANG G, *et al*. Porosity modulated high-performance piezoelectric nanogenerator based on organic/inorganic nanomaterials for self-powered structural health monitoring. *ACS Applied Materials & Interfaces*, 2020, **12(42):** 47503.

[16] BAGHALI M, JAYATHILAKA W, RANAKRISHNA S. The role of electrospun nanomaterials in the future of energy and environment. *Materials*, 2021, **14(3):** 558.

[17] LU L, DING W, LIU J, *et al*. Flexible PVDF based piezoelectric nanogenerators. *Nano Energy*, 2020, **78:** 105251.

[18] LUO X, WANG Z, YAN M, *et al*. One-pot three-step synthesis of PDMAEMA-b-PMMA-b-PNIPAM triblock block copolymer for preparing pH and thermal dual-responsive PVDF blend membranes. *Polymer Engineering and Science*, 2023, **63(10):** 3343.

[19] YANG X R, WANG R Y, WANG H J, *et al*. A robust-switchable poly(vinyl alcohol) gel with adjustable multiple hydrogen bonding interactions. *European Polymer Journal*, 2023, **195:** 112192.

[20] SONG Y, SHI Z, HU G H, *et al*. Recent advances in cellulose-based piezoelectric and triboelectric nanogenerators for energy harvesting: a review. *Journal of Materials Chemistry A*, 2021, **9(4):** 1910.

[21] CAUDA V, STASS S, BEJTKA K, *et al*. Nanoconfinement: an effective way to enhance PVDF piezoelectric properties. *ACS Applied Materials & Interfaces*, 2013, **5(13):** 6430.

[22] DALLAEV R, PISARENKO T, SOBOLA D, *et al*. Brief review of PVDF properties and applications potential. *Polymers*, 2022, **14(22):** 4793.

[23] WEI S, WANG X, ZHAO X, *et al*. Detection of pesticide residues on flexible and transparent fluorinated polyimide film based on surface-enhanced Raman spectroscopy technology. *Analytica, Chimica Acta*, 2023, **1283:** 341958.

[24] HU R, ZHAO J, ZHU G, *et al*. Fabrication of flexible free-standing reduced graphene oxide/polyaniline nanocomposite film for all-solid-state flexible supercapacitor. *Electrochimica Acta*, 2018, **261:** 151.

[25] LI C, XU S, YU J, *et al*. 3D hybrid MoS_2/AgNPs/inverted pyramid PMMA resonant cavity system for the excellent flexible surface enhanced Raman scattering sensor. *Sensors and Actuators B-Chemical*, 2018, **274:** 152.

[26] MAGDY G, HASSANIN A H, KANDAS I, *et al*. PVDF nanostructures characterizations and techniques for enhanced piezoelectric response: a review. *Materials Chemistry and Physics*, 2024, **325:** 129760.

[27] HE Z, RAULT F, LEWANDOWSKI M, *et al*. Electrospun PVDF nanofibers for piezoelectric applications: a review of the influence of electrospinning parameters on the *β* phase and crystallinity enhancement. *Polymers*, 2021, **13(2):** 174.

[28] LI Y, HU Q, ZHANG R, *et al*. Piezoelectric nanogenerator based on electrospinning PVDF/cellulose acetate composite membranes for energy harvesting. *Materials*, 2022, **15(19):** 7026.

[29] VENKATESAN M, CHEN W C, CHO C J, *et al*. Enhanced piezoelectric and photocatalytic performance of flexible energy harvester based on $CsZn_{0.75}Pb_{0.25}I_3$/CNC-PVDF composite nanofibers. *Chemical Engineering Journal*, 2022, **433:** 133620.

[30] CHENG Y, FENG Y, PAN Z, *et al*. Multilayer nanocomposites with ultralow loadingsof nanofillers exhibiting superb capacitive energy storage performance. *Energy & Environmental Science*, 2023, **16(12):** 5881.

[31] HU P, YAN L, ZHAO C, *et al*. Double-layer structured PVDF nanocomposite film designed for flexible nanogenerator exhibiting enhanced piezoelectric output and mechanical property. *Composites Science and Technology*, 2018, **168:** 327.

[32] SUN Z, XIN H, DIWU L, *et al*. Boosting the energy storage performance of BCZT-based capacitors by constructing a Schottky contact. *Materials Horizons*, 2025, **12(7):** 2328.

[33] SUN Z, BAI Y, JING H, *et al*. A polarization double-enhancement strategy to achieve super low energy consumption with ultra-high energy storage capacity in BCZT-based relaxor ferroelectrics. *Materials Horizons*, 2024, **11(14)**: 3330.

[34] SUN Z, ZHAO S, WANG T, *et al*. Achieving high overall energy storage performance of KNN-based transparent ceramics by ingenious multiscale designing. *Journal of Materials Chemistry A*, 2025, **12(27):** 16735.

[35] SUN Z, WANG Z, TIAN Y, *et al*. Progress, outlook, and challenges in lead-free energy-storage ferroelectrics. *Advanced Electronic Materials*, 2020, **6(1):** 1900698.

[36] SUN Z, BAI Y, LIU J, *et al*. Interface engineering in ferroelectrics: from films to bulks. *Journal of Alloys and Compounds*, 2022, **909:** 164735.

[37] JI X, WANG C, HARUMOTO T, *et al*. Structure and electrical properties of BCZT ceramics derived from microwave-assisted Sol-Gel-hydrothermal synthesized powders. *Scientific Reports*, 2020, **10(1):** 20352.

[38] CHUKHCHIN D G, MALKOV A V, TYSHUNOVA I V, *et al*. Diffractometric method for determining the degree of crystallinity of materials. *Crystallography Reports*, 2016, **61(3):** 371.

[39] DANG S T, XUE L L, HE L F, *et al*. Dielectric and energy storage properties of $Ba_{0.85}Ca_{0.15}Zr_{0.1}Ti_{0.9}O_3$ ceramics with different aging temperature during the Sol-Gel process. *Journal of Materials Science: Materials in Electronics*, 2022, **33(35):** 26100.

[40] KOU Q, YANG B, SUN Y, *et al*. Tetragonal (Ba, Ca)(Zr, Ti)O_3 textured ceramics with enhanced piezoelectric response and superior temperature stability. *Journal of Materiomics*, 2022, **8(2):** 366.

[41] CHAKKCHAOUI N, FARHAN R, BOUTALDAT M, *et al*. Piezoelectric *β*-polymorph formation of new textiles by surface modification with coating process based on interfacialinteraction on the conformational variation of poly (vinylidene fluoride) (PVDF) chains. *The European Physical Journal Applied Physics*, 2020, **91(3):** 31301.

[42] SUN Z, LIU J, WEI H, *et al*. Ultrahigh energy storage capacity in multilayer-structured cellulose-based dielectric capacitors caused by interfacial polarization-coupled Schottky barrier height. *Journal of Materials Chemistry A*, 2023, **11(37):** 20089.

[43] SUN Z, WEI H, ZHAO S, *et al*. Utilizing the synergistic effect between the Schottky barrier and field redistribution to achieve high-density, low-consumption, cellulose-based flexible dielectric films for next-generation green energy storage capacitors. *Journal of Materials Chemistry A*, 2024, **12(1):** 128.

[44] SUN Z, WANG S, ZHAO S, *et al*. Achieving low energy consuming bio-based piezoelectric nanogenerators *via* modulating the inner layer thickness for a highly sensitive pedometer. *Journal of Materials Chemistry C*, 2024, **12(3):** 859.

[45] OTTA S, KAND L, DAS R K, *et al*. Piezoelectric, structural, vibration and optical properties of lead free based $0.5Ba(Ti_{0.8}Zr_{0.2})O_3$–$0.5(Ba_{0.7}Ca_{0.3})TiO_3$ ceramic sample. *Materials Today Communications*, 2023, **35:** 106191.

[46] JI W, FANG B, LU X, *et al*. Tailoring structure and performance of BCZT ceramics prepared *via* hydrothermal method. *Physica B: Condensed Matter*, 2019, **567:** 65.

[47] LIU Y, PU Y, SUN Z, *et al*. Enhanced relaxor ferroelectric behavior of BCZT lead-free ceramics prepared by hydrothermal method. *Materials Letters*, 2014, **137:** 128.

[48] BARASKAR B G, KOLEKAR Y D, THOMBARE B R, *et al*. Enhanced piezoelectric, ferroelectric, and electrostrictive properties of lead-free (1–*x*)BCZT–*x*BCST electroceramics with energy harvesting capability. *Small*, 2023, **19(37):** 2300549.

[49] MISSAOUI S, BOUHAMED A, NOURI H, *et al*. Sustainable and flexible piezoelectric nanogenerator with hybrid nanocomposites based on high-performance synthesized BCZT powder. *ACS Applied Electronic Materials*, 2024, **6(8):** 5608.

[50] LI Y, TAN J, LIANG K, *et al*. Enhanced piezoelectric performance of multi-layered flexible polyvinylidene fluoride-$BaTiO_3$-rGO films for monitoring human body motions. *Journal of Materials Science: Materials in Electronics*, 2022, **33(7):** 4291.

[51] RAVINDRAN P, VIDYA R, KJEKSHUS A, *et al*. Theoretical investigation of magnetoelectric behavior in $BiFeO_3$. *Physical Review B-Condensed Matter and Materials Physics*, 2006, **74(22):** 224412.

[52] YANG P, ZHAO L, SHI S, *et al*. The influence of interface on the dielectric and tunable properties of BCZT/BZT ceramic. *Journal of Materials Science: Materials in Electronics*, 2024, **35(8):** 610.

[53] JI D, ZHANG M, SUN H, *et al*. Enhanced mechanical and dielectric properties of lignocellulosic composite papers with biomimetic multilayered structure and multiple hydrogen-bonding interactions. *International Journal of Biological Macromolecules*, 2024, **281:** 136247.

[54] HANANI Z, MEZZANE D, AMIOUD M, *et al*. Structural, dielectric, and ferroelectric properties of lead-free BCZT ceramics elaborated by low-temperature hydrothermal processing. *Journal of Materials Science: Materials in Electronics*, 2020, **31(13):** 10096.

[55] JAFFARI G H, SHAWANA H, MUMTAZ F, *et al*. Electrical response of PVDF/$BaTiO_3$ nanocomposite flexible free-standing films. *Bulletin of Materials Science*, 2023, **46(4):** 227.

[56] SU C, HUANG X, ZHANG L, *et al*. Robust superhydrophobic wearable piezoelectric nanogenerators for self-powered body motion sensors. *Nano Energy*, 2023, **107:** 108095.

[57] ZHANG Y, RUAN K, GU J. Flexible sandwich-structured electromagnetic interference shielding nanocomposite films with excellent thermal conductivities. *Small*, 2021, **17(42):** 2101951.

通过双相 BCZT 掺杂策略实现纸基压电纳米发电机的高功率密度

王斯婷[1], 孙梓雄[1], 刘鑫莹[1], 韩沛桥[1], 汪秀丽[2], 张素风[3]

(1. 陕西科技大学 电子信息与人工智能学院, 西安 710021; 2. 环境友好高分子材料教育部工程研究中心(四川大学), 成都 610065; 3. 陕西科技大学 轻工科学与工程学院, 西安 710021)

摘 要: 高性能柔性压电纳米发电机(Piezoelectric nanogenerator, PENG)的发展对自供能传感和微电子器件的应用具有重要意义。本研究采用氢键替换策略, 制备了基于纤维素/聚偏二氟乙烯(PVDF)共混薄膜的多层 PENG, 并引入多相 BCZT($0.1BaZr_{0.2}Ti_{0.8}O_3$-$0.9Ba_{0.7}Ca_{0.3}TiO_3$)陶瓷填料以优化其性能。SEM 和 TEM 表征结果表明, 复杂的氢键网络有效促进陶瓷填料在复合薄膜亚层中分散均匀。为探究填料分布对 PENG 性能的影响, 本研究制备并对比了单层与双层复合薄膜结构。结果表明, 双层 PENG 的电学输出性能显著优于单层结构, 其中 D-L_3H_7 构型的开路电压(Open circuit voltage, V_{OC})达 23.13 V, 短路电流(Short circuit current, I_{SC})达 8.32 μA。这一性能提升归因于增大的层间界面有效抑制了电荷注入与迁移, 从而提高了电荷密度。此外, 具有尖锐顶角的六方/四方相陶瓷纳米颗粒进一步诱导了局部电场增强效应, 优化了器件的压电转换性能。

关 键 词: 压电纳米发电机; 纤维素; BCZT; 氢键工程策略

中图分类号: TM619 **文献标志码:** A **文章编号:** 1000-324X(2026)01-0129-08

Supporting Materials

Achieving High Power Density in Paper-based Piezoelectric Nanogenerators through Dual-phase BCZT Doping Strategy

WANG Siting[1], SUN Zixiong[1], LIU Xinying[1], HAN Peiqiao[1], WANG Xiuli[2], ZHANG Sufeng[3]

(1. School of Electronic Information and Artificial Intelligence, Shaanxi University of Science and Technology, Xi'an 710021, China; 2. Engineering Research Center of Eco-friendly Polymeric Materials, Ministry of Education, (Sichuan University), Chengdu 610065, China; 3. College of Bioresources Chemical & Materials Engineering, Shaanxi University of Science and Technology, Xi'an 710021, China)

S1 Experimental

S1.1 Fabrication of the BCZT@cellulose/PVDF precursors

Materials used in the experiment are as follows. The cellulose comes from the cotton linter purchased from Hubei Jinhuan New Material Technology Co., Ltd. The DMAc (99.0%), LiCl (99.0%), PVDF (average Mw ~534000 $g \cdot mol^{-1}$), $BaCO_3$ (99.0%), $CaCO_3$ (99.0%), ZrO_2 (99.0%) and TiO_2 (98.0%) were all purchased from Sinopharm Chemical Reagent Co., Ltd. Barium calcium zirconate titanate ($0.1BaZr_{0.2}Ti_{0.8}O_3$–$0.9Ba_{0.7}Ca_{0.3}TiO_3$), abbreviated as BCZT, was synthesized as follows. Based on its chemical formula indices, appropriate amounts of barium titanate, calcium titanate, zirconium oxide, and titanium oxide were weighed and added to zircon, followed by ball milling for 12 h. After sieving and drying, BCZT powder was obtained and then fired in a muffle furnace at 1100 and 1300 ℃ for 6 h each, with a heating rate of 3 ℃/min. The samples fired at higher and lower temperatures were named BCZT-H and BCZT-L, respectively. The double powders were ground and sieved through a 120-mesh (ϕ0.125 mm) screen to get BCZT ceramic particles. The BCZT@cellulose/PVDF precursor was prepared referring to our previous work. Firstly, cellulose was activated in a DMAc aqueous solution by stirring at 160 ℃ for 30 min. Subsequently, it was extracted and placed in a LiCl aqueous solution with a mass ratio of cellulose (s)/DMAc (l)/LiCl (s) of 2 : 51 : 5. The solution was stirred again at 100 ℃ for 3 h and left to stand for 24 h to yield a transparent cellulose solution. Meanwhile, a mixture of PVDF (s), DMAc (l), and LiCl (s) at a mass ratio of 3 : 51 : 5 was stirred at 50 ℃ for 6 h to obtain a PVDF solution. The two solutions were mixed at a cellulose/PVDF mass ratio of 80/20, and 2% (volume fraction) BCZT ceramic particles were added. All ternary solutions were stirred for at least 12 h until uniform. Finally, the mixture was stirred for 30 min under ultrasonic oscillation-assisted magnetic stirring, repeated 5 times, to obtain different BCZT@cellulose/PVDF precursors.

S1.2 Preparation of BCZT@cellulose/PVDF composite film

Composite films with one or double layers can be fabricated *via* the tape-casting method using the aforementioned precursor solutions. In our work, unlike conventional approaches, each layer is casted before the previous one is fully dried. This enables the interaction of the hydrogen bond network between adjacent layers, which is more active in a liquid environment, facilitating the formation of a multilayer structure and interface flattening. It should be emphasized that there aren't many complex scientific issues in this process, yet several attempts may be needed to determine the optimal time for casting the next layer. We prepared two structures: single-layer and double-layer composite films. Due to the varying contents of BCZT ceramic particles fired at different temperatures, the single-layer composite films are named as follows: S-H, S-L, S-L_3H_7, S-L_5H_5, S-L_7H_3 (where S-H indicates that all 2% (volume fraction) BCZT ceramic particles added in the singlee-layer composite film are fired under high temperature conditions, and for S-L_3H_7, it means that in the single-layer composite film, the ratio of low to high temperature fired BCZT ceramic particles is 3 : 7, and the naming principle is similar for the others). The double-layer composite films are named D-L_3H_7, D-L_5H_5, and D-L_7H_3.

S1.3 Fabrication of PENGs

Composite films were cut into 1.5 cm radius circles, with conductive copper tapes and wires affixed to both sides. An outer protective layer was essential to bolster device stability and shield against external mechanical stress, temperature, and humidity. PDMS curing agent and accelerator were mixed at a 10 : 1 ratio and stirred for 30 min. Subsequently, the mixture was placed in a 0.8 kPa vacuum drying oven to eliminate liquid bubbles. The composite film, equipped with copper electrodes and wires, was then immersed in a container. An appropriate

amount of the PDMS solution was poured in until the film was fully covered. After standing briefly, once the PDMS on the film surface had completely solidified, a PENG was obtained.

S1.4 Characterization

For a comprehensive understanding of the materials and devices in this study, a series of advanced characterization techniques were meticulously employed. The crystal structures of BCZT-H and BCZT-L ceramic particles were determined *via* X-ray diffraction (XRD, Rigaku Co., Tokyo, Japan). The XRD scans, 2θ spanning from 10° to 80°, were executed at a scanning rate of 2 (°)/min over a period of 2 h, enabling accurate phase identification. To explore the microstructural features of the composite films, both scanning electron microscope (SEM, Thermo Fisher Scientific) and field emission transmission electron microscope (FE-TEM, JEOL, JEM-F200) were utilized. These techniques provided detailed insights into the surface morphology and cross-sectional characteristics. Fourier transform infrared spectroscopy (FT-IR, Spotlight 400 & Frontier) was adopted to acquire IR spectra in the range of 400–1000 cm^{-1} with a 1 cm^{-1} resolution, crucial for identifying functional groups in the composite films. For electrical property evaluation, 1-mm-diameter electrodes were sputtered on both sides of the films. The ferroelectric test system equipped with an impedance analyzer (E4980A, Agilent) measured the frequency and temperature-dependent dielectric constant (ε) and dielectric loss (tanδ). A ferroelectric tester (Radiant Premier II) recorded *J-E* curves and *P-E* loops at 100 Hz. Mechanical properties were determined using a servo-controlled universal testing machine (AI-7000-NGD, Gotech Testing Machines), and hydrophobicity was assessed *via* water-contact angle measurements. Finally, the short circuit current (I_{SC}) and open circuit voltage (V_{OC}) of the BCZT@cellulose/PVDF composite PENG were precisely recorded by a Keithley 2450 source meter.

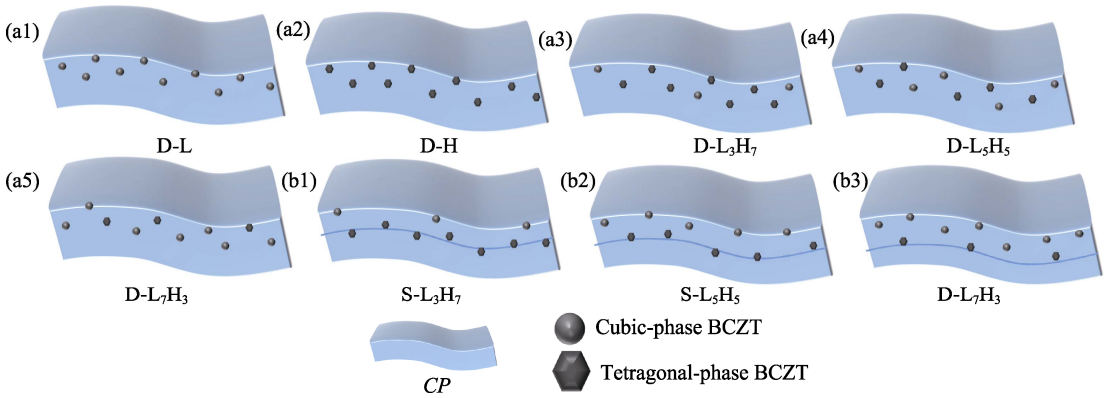

Fig. S1 Schematic diagrams of composite films with different structures

(a1-a5) Schematic diagrams of double-layer composite films; (b1-b3) Schematic diagrams of single-layer composite films

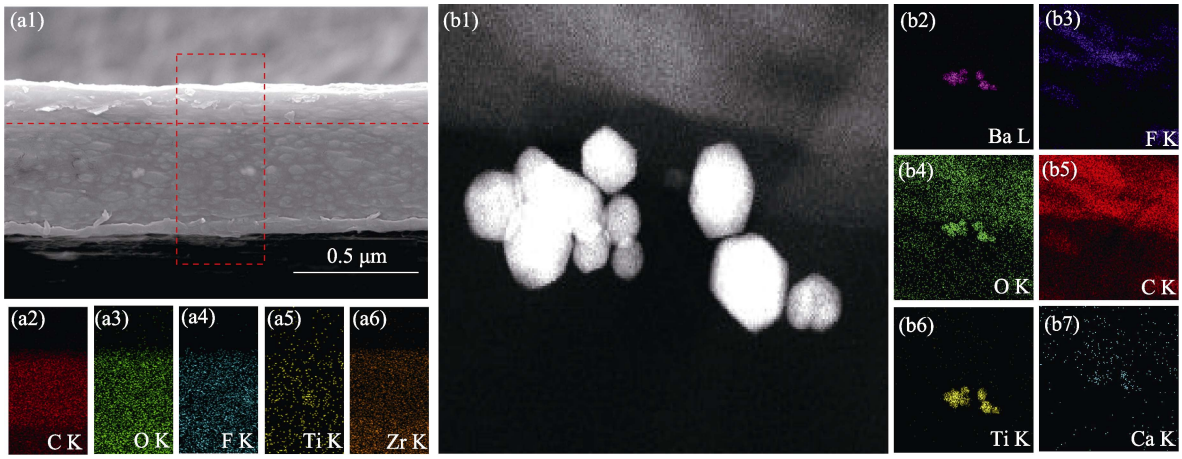

Fig. S2 Morphological structure of the BCZT@cellulose/PVDF composite film

(a1) SEM image of the general area of the D-L_3H_7 film; (a2-a6) EDS images of C, O, F, Ti, and Zr in Fig. (a1); (b1) TEM image of the general area of the D-L_3H_7 film; (b2-b7) EDS images of Ba, F, O, C, Ti, and Ca in Fig. (b1)

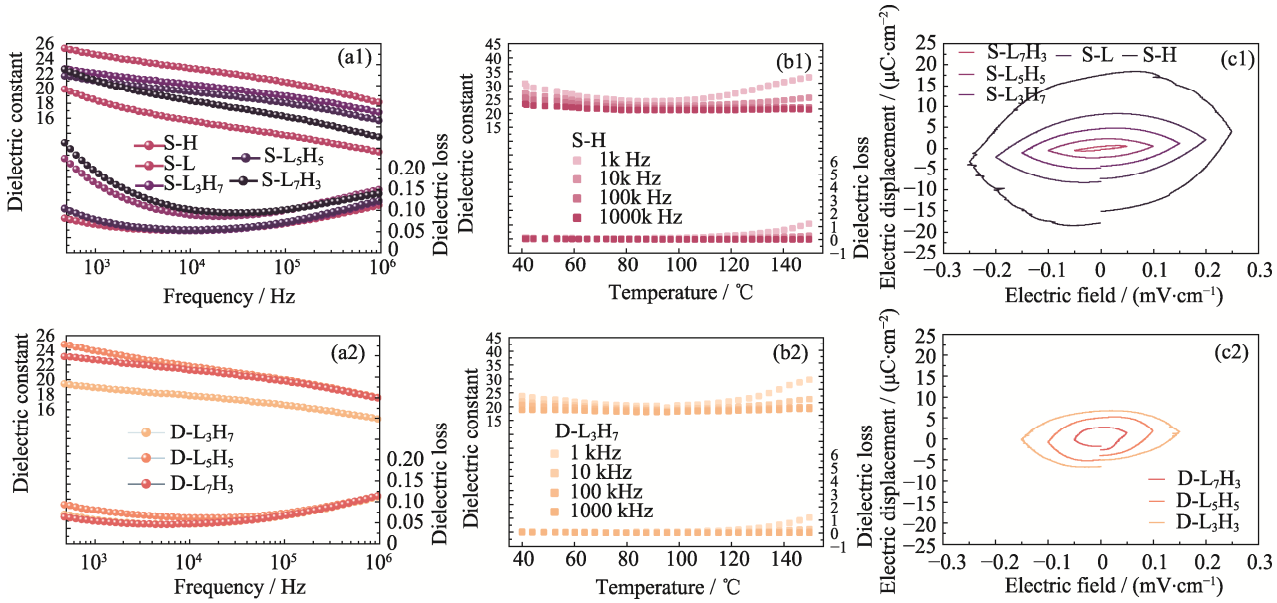

Fig. S3　Electrical performance tests of PENGs with different configurations

(a1, a2) Frequency dependence of ε and tanσ of (a1) all single-layered films and (a2) all double-layered films; (b1, b2) Temperature dependence of ε and tanσ of (b1) S-H and (b2) D-L$_3$H$_7$; (c1, c2) *P*–*E* loops of (c1) all single-layered films and (c2) all double-layered films

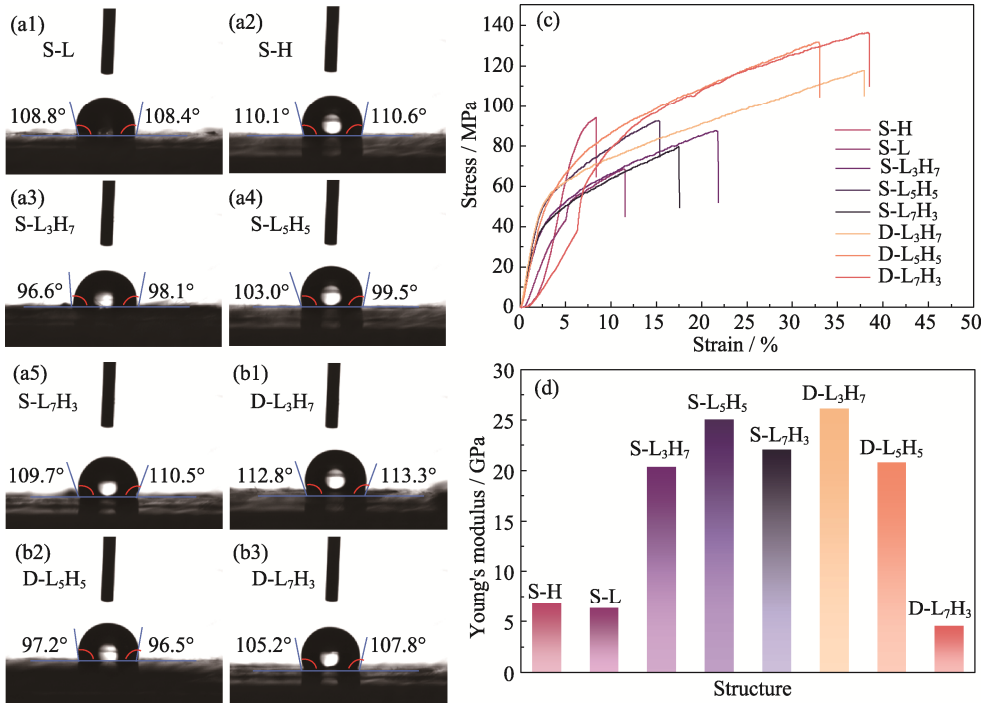

Fig. S4　Water contact and mechanical property of different thin films

(a1-a5) Water contact angles for single-layer filmss; (b1-b3) Water contact angles for double-layer films; (c) Stress-strain curves and (d) corresponding Young's modulus

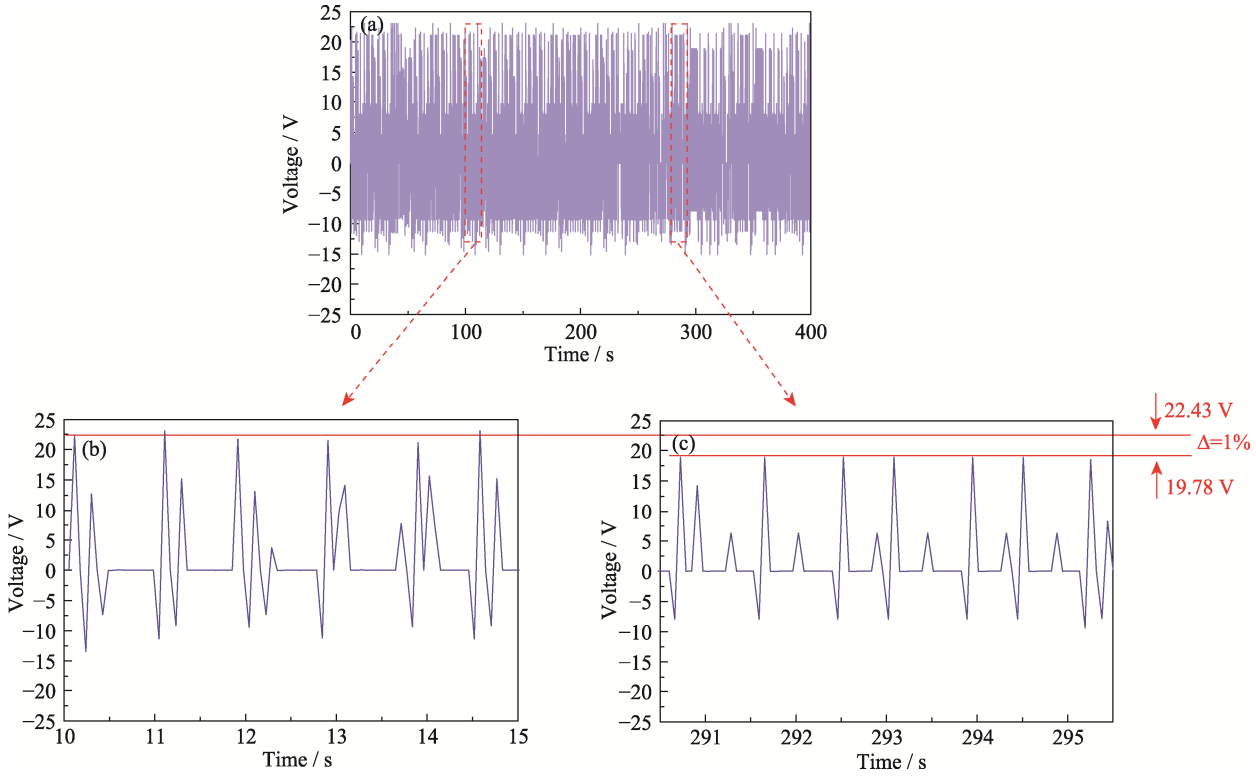

Fig. S5 Durability test of the D-L_3H_7 PENG
(a) 400 s; (b, c) Partially enlarged views of Fig. (a)

Table S1 Serial number and performance of single-layer PENG

Single-layer-structured PENG (number)	BCZT-L : BCZT-H	V_{OC}/V	I_{SC}/μA	P_D/(μW·cm^{-2})
S-H	0 : 1	19.31	4.42	11.33
S-L_3H_7	3 : 7	15.63	3.17	6.58
S-L_5H_5	5 : 5	12.55	2.25	3.82
S-L_7H_3	7 : 3	7.52	1.18	1.17
S-L	1 : 0	5.23	0.88	0.57

Table S2 Serial number and performance of double-layer PENG

Double-layer-structured PENG (number)	BCZT-L : BCZT-H	V_{OC}/V	I_{SC}/μA	P_D/(μW·cm^{-2})
D-L_3H_7	3 : 7	23.13	8.32	26.06
D-L_5H_5	5 : 5	17.53	6.71	14.45
D-L_7H_3	1 : 0	6.20	1.85	1.57